Photogrammetric Processing of Tianwen-1 HiRIC Imagery for Precision Topographic Mapping on Mars

Zhaojin Li, Bo Wu, Wai Chung Liu, Long Chen, Hongliang Li, Jie Dong, Wei Rao, Dong Wang, Qingyu Meng, and Jihong Dong

***Abstract*— The high-resolution imaging camera (HiRIC) onboard China's Tianwen-1 Mars probe aims to acquire detailed imagery of the Martian surface to comprehensively investigate its topography and geomorphology. The HiRIC is a pushbroom camera comprising three CCDs to simultaneously achieve submeter resolution and a large swath. However, processing HiRIC images using the conventional photogrammetric workflow is difficult due to the large shifts and narrow overlapping among the CCD lines. This article presents a novel approach for photogrammetric processing of HiRIC images for precision topographic mapping that incorporates: 1) the fitting of the initial rational polynomial coefficients (RPCs) of images from the HiRIC position and pointing data; 2) a deep-learning-based method for tie-point matching between adjacent CCD images and cross-orbit images; 3) the bundle adjustment of multiple CCD images for tripled-epipolar image generation to ensure inner orbit consistency; 4) the block adjustment of multiple orbit images to ensure cross-orbit consistency; and 5) dense image matching and space intersection based on the refined RPCs to generate digital elevation models (DEMs). Experimental analyses were conducted using HiRIC images covering the landing region of the Zhurong rover. The results revealed that subpixel accuracy was achieved for image residuals among multiple-CCD or multiple-orbit images. Comparison with the reference data (HiRISE and MOLA DEMs) revealed a mean deviation of less than 7 m in terms of the geometric accuracy and the subtle topographic details of the HiRIC DEM. The presented approach offers a reliable solution for using the new dataset of HiRIC imagery for Mars topographic mapping.**

***Index Terms*— Bundle adjustment, digital elevation model (DEM), high-resolution imaging camera (HiRIC), Mars, Tianwen-1.**

I. Introduction

CHINA'S first Mars probe, the Tianwen-1 carrying the Zhurong rover, was launched in July 2020, entered the Martian orbit in February 2021, and successfully landed Zhurong in southern Utopia Planitia in May 15, 2021 [1]–[3]. From mid-February to early May 2021, the Tianwen-1 orbiter performed detailed investigations of the potential landing region in southern Utopia Planitia using its onboard instruments. Among these investigations, images obtained by the high-resolution imaging camera (HiRIC) were used for high-precision and high-resolution 3-D topographic mapping to facilitate the selection of the best landing site for the Zhurong rover [3] and provide data support for various scientific studies [4].

The global-scale topographic product from the Mars Orbiter Laser Altimeter (MOLA) [5], [6] is publicly available; however, its 463-m/pixel resolution could not satisfy the requirements for landing site hazard assessment. High-resolution images, such as those acquired by the high-resolution imaging experiment (HiRISE) onboard the Mars Reconnaissance Orbiter (MRO), feature submeter resolution, providing sufficient details for topographic mapping [7]. However, the field of view and coverage of HiRISE images are inevitably small and could not be used for large-scale topographic mapping and analyses. The HiRISE images cover only a small portion of the candidate landing region of the Zhurong rover before its landing [2].

The HiRIC onboard the Tianwen-1 orbiter is a pushbroom camera that can achieve high-resolution imaging (0.5 m/pixel at an altitude of 265 km) with a focal length of 4640 mm [8]. The HiRIC contains three charge-coupled devices (CCDs), named CCD1, CCD2, and CCD3, on the same focal plane to achieve a swath of up to 9 km. There are small offsets between any two adjacent CCDs perpendicular to the flying direction. Moreover, CCD2 in the middle has an offset of 0.47° (equal to more than 4000 pixels) with the other two CCDs along the flying direction, which cannot form a unified image with the other two CCDs for photogrammetric processing. With respect to stereo imaging, the HiRIC adopts a side-slewing stereo strategy by revisiting the region at a 22° convergent angle. However, the overlapping region between the stereo pair is uncertain because it includes six CCD images, each 6144 pixels wide and more than 240 000 pixels long. In addition, the overlapping region between adjacent CCDs is as narrow as approximately140 pixels, which makes it difficult to preserve the internal consistency of multiple CCD images within one orbit. A straightforward photogrammetric method is to individually process the stereo pairs of each CCD image.

Manuscript received 10 February 2022; revised 23 June 2022; accepted 22 July 2022. Date of publication 26 July 2022; date of current version 8 August 2022. This work was supported in part by a grant from the China Academy of Space Technology under Project 17CPIT/HK0103 and in part by the grants from the Research Grants Council of Hong Kong under RIF Project R5043-19, Project PolyU 15210520, and Project PolyU 15219821. *(Corresponding author: Bo Wu.)*

Zhaojin Li, Bo Wu, Wai Chung Liu, Long Chen, and Hongliang Li are with the Department of Land Surveying and Geo-Informatics and the Research Centre for Deep Space Explorations, The Hong Kong Polytechnic University, Hong Kong (e-mail: bo.wu@polyu.edu.hk).

Jie Dong and Wei Rao are with the China Academy of Space Technology, Beijing 100081, China.

Dong Wang, Qingyu Meng, and Jihong Dong are with the Changchun Institute of Optics, Fine Mechanics and Physics, Chinese Academy of Sciences, Changchun 130033, China.

Digital Object Identifier 10.1109/TGRS.2022.3194081

However, this approach will lead to the following problems: 1) gaps of varying sizes will be inevitable as a stereo pair of orbit images involves at least three stereo pairs of CCD images, complicating the stereo overlapping of the individual CCD images; 2) geometric inconsistencies among the individual stereo pairs of CCD images will arise; and 3) if the internal consistency among the three CCD images in each orbit is not guaranteed, the block adjustment of multiple-orbit HiRIC images is not likely to yield proper results, as inconsistencies will be propagated and accumulated.

For precision topographic mapping on Mars using the HiRIC images, this article presents a novel photogrammetric approach to address the challenges described above. First, rational polynomial coefficients (RPCs) of each CCD image are fit from the HiRIC position and pointing data, serving as initial values for the bundle adjustment and facilitating the tie-point matching. A state-of-the-art deep-learning method [9] is used for tie-point matching, providing sufficient tie points even in the narrow overlapping regions between the adjacent CCD images. Next, the bundle adjustment of multiple CCD images is conducted based on the tie points to obtain improved RPCs, from which a tripled-epipolar image can be generated to merge the three CCD images into a single image in the epipolar plane, enabling integrated processing of the three CCD images to maintain their internal consistency. A block adjustment of multiple-orbit images is then conducted to improve cross-orbit consistency. Finally, dense image matching is performed to generate 3-D point clouds for the interpolation of digital elevation models (DEMs).

The remainder of this article is organized as follows. Section II reviews the recent developments in Mars topographic mapping. Section III describes the proposed photogrammetric method for precise topographic mapping using HiRIC images. Section IV presents a systematic experimental evaluation of the proposed method using HiRIC images covering the Zhurong landing region. Section V contains the discussion and conclusions.

II. Related Works

Previous Mars exploration missions have obtained tremendous datasets for Mars topographic mapping. Representative examples include the high-resolution stereo camera (HRSC) onboard the Mars Express [10] and the HiRISE onboard the MRO [11]. The HRSC has a unique along-track stereo configuration with an imaging resolution of up to 12.5 m/pixel. The HRSC has almost completed global imaging after more than 20 years in operation. The HiRISE has the best imaging resolution of 0.3 m/pixel but limited spatial coverage on Mars. Topographic maps obtained from these datasets are essential for the engineering operations of landing missions and various scientific studies on Mars.

The Martian surface is topographically mapped from images using two main types of methods: photogrammetry and photoclinometry [12]. Photogrammetry, based on the rigorous mathematic formula of collinearity [13], is the predominant method for 3-D topographic mapping from stereo images. In general, the photogrammetric process involves two main steps: bundle adjustment to improve image orientation parameters and dense image matching to obtain 3-D point clouds for DEM interpolation. Unlike images of Earth, which have relatively accurate exterior orientation (EO) parameters provided by GPS/IMU, the EO parameters of images of other planets are usually interpolated from the ephemeris and pointing data of the spacecraft. The positional parameters may contain errors of up to 2 km [14] due to errors in long-distance signal transmission and measurement, the oscillation of the spacecraft, and other uncertainties. Bundle adjustment, thus, intends to improve the EO parameters of images, enforce consistency with the reference datum, and eliminate inconsistencies among images. Tie points across images are crucial for guaranteeing bundle adjustment performance. Generally, scale-invariant feature transform (SIFT)-like feature detectors [15] can handle regular stereo images, yielding abundant tie points for bundle adjustment [16]. However, some special cameras, such as the HiRISE, bundle multiple high-resolution CCDs on the same image plane to simultaneously achieve high-resolution imaging and a large swath, which requires matching tie points within a narrow overlapping region between the CCDs. Hu and Wu [17] proposed using the initial orientation parameters of images to match tie points for images with narrow overlapping regions. However, this method requires the extraction of abundant feature points and sufficient accuracy of the initial orientation parameter to estimate the overlapping regions of the images. Recent advances in deep-learning-based image matching [9], [18] have remarkably improved tie-point matching. Deep-learning algorithms typically obtain the pixelwise or featurewise descriptor using a convolutional neural network (CNN) and train the network for use. Applying a supervision strategy in training, deep-learning-based matching algorithms can omit the matching filtering step and output more robust matching results, even for narrowly overlapping images.

For most of the pushbroom cameras, the changes in platform position and attitude angles during imaging can be modeled using second-order, third-order, or Lagrange polynomials, establishing the relationship between the 2-D pixel coordinates and the 3-D object coordinates using collinearity equations. For instance, Li *et al.* [19] used third-order polynomials to model the EO parameters for the photogrammetric processing of HiRISE images. Li *et al.* [20] used second-order polynomials to model the EO parameters to process HRSC images. In these methods, the EO parameters possess physical meanings that are convenient for modeling different types of error (e.g., image distortion, gyro drift, and position bias). Nevertheless, as the correspondence between the object point and the specific EO parameters (corresponding to a specific image line) is unknown, iteration to determine the correct EO parameters is unavoidable [21]. Alternatively, the widely used rational function model, based on RPCs [22] and rigorously derived from the above mathematical model, was proposed to project the 3-D points onto the 2-D images directly. Although RPCs do not possess specific physical meanings, the adjustable parameters in bundle adjustment can absorb various error types, yielding refined RPCs.

For dense image matching, least-squares matching (LSM) has become the *de facto* standard due to its capability in

achieving subpixel precision and flexibility in implementing more constraints [10]. However, the pixelwise calculation requires high computational costs, especially for planetary images of large sizes. Hirschmuller [23] proposed semiglobal matching (SGM), achieving a favorable performance for 3-D reconstruction from pushbroom images at a reduced computational cost. By transforming the global problem into a dynamic programming problem from multiple directions, pixelwise disparities can be achieved in SGM. To address the inherent smoothness issue in SGM, Hu *et al.* [24] further proposed a texture-aware SGM using an edge detection algorithm to extract edges and adaptively modify the penalties.

Photoclinometry, or shape-from-shading, is a 3-D reconstruction method that exploits the shading information on images and imaging principles to excavate the underlying information behind each gray value [25]. Photoclinometry can theoretically recover the 3-D information for each observed pixel on an image to achieve pixelwise reconstruction, even for regions with weak textures, such as the surfaces of the moon and Mars. Photoclinometry has been successfully used for lunar topographic mapping in recent years [12], [26], [27]. However, the atmosphere of Mars complicates photoclinometric processing by introducing optical depth, scattering factors, and other influences. Li *et al.* [20] proposed an effective photoclinometric method to process HRSC images for pixelwise 3-D mapping using a DEM derived from photogrammetry as the initial input and taking advantage of the triplet HRSC images to provide additional observations to model the atmospheric parameters. However, photoclinometric 3-D mapping remains an open research topic for Mars images from other sources.

Similar to the HiRISE with over ten CCDs mounted on the same focal plane [11], the HiRIC onboard the Tianwen-1 orbiter has three CCDs mounted on the same focal plane to achieve high-resolution imaging with a large swath. However, the large offset (more than 4000 pixels) between CCD2 and the other two CCDs along the flying direction complicates the photogrammetric processing of HiRIC images. Therefore, innovative photogrammetric methods must be developed for precision topographic mapping using the HiRIC images.

III. Rigorous Photogrammetric Processing of HiRIC Images

A. Overview of the Approach

Fig. 1 shows the overall workflow of the proposed approach for the photogrammetric processing of HiRIC images. First, the RPCs of each CCD image are fit from the position and pointing data of the HiRIC to establish the direct relationship between the 2-D image coordinates and 3-D object coordinates. A state-of-the-art deep-learning method [9] is used for tie-point matching within the narrow overlapping region between the adjacent CCD images and in the overlapping images from multiple orbits. The bundle adjustment of multiple CCD images is conducted based on the tie points to obtain improved RPCs, from which a tripled-epipolar image can be generated to merge the three CCD images of each orbit into one image in the epipolar plane. Next, a multiple-orbit image block adjustment is performed to improve the cross-orbit consistency while maintaining the internal consistency of each orbit image. Finally, SGM [23] and LSM for subpixel refinement are performed to obtain pixelwise disparities from the epipolar images, from which 3-D point clouds can be generated using the refined RPCs via space intersection, enabling DEM generation.

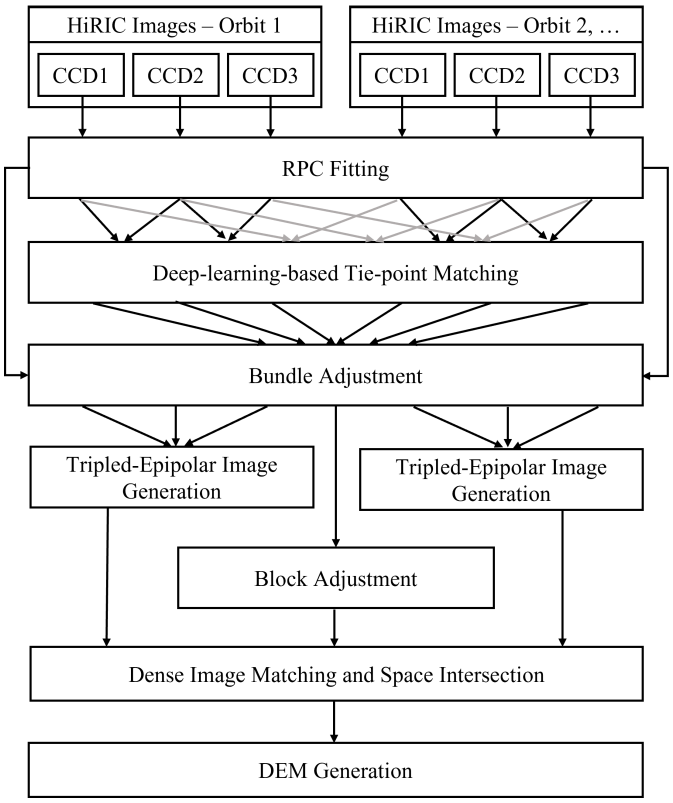

Fig. 1. Workflow of the proposed method for the photogrammetric processing of HiRIC images.

B. HiRIC Imaging Geometry and Nominal RPC Generation

The HiRIC is a pushbroom camera with three CCD arrays, each comprising a panchromatic line and four colored lines (near-infrared, red, green, and blue) [8], as shown in Fig. 2. The HiRIC has a spatial resolution of 0.5 m/pixel at an altitude of 265 km. With 6144 pixels in each CCD line, more than 18 000 pixels can be obtained by combining the three CCD lines to provide a swath of approximately 9 km. However, CCD2 has an offset of 0.47° (equal to more than 4000 pixels) with the other two CCDs along the flying direction [see Fig. 2(a)]. Two additional moderate resolution cameras (MoRICs) are placed on the same imaging plane to simultaneously capture images/videos at a 10 m/pixel resolution. To obtain stereo images for photogrammetric processing, the HiRIC adopts a side-slewing strategy by revisiting the same region to form a 22° convergent angle, as illustrated in Fig. 2(b). The detailed parameters of the HiRIC are listed in Table I.

Regarding the interior orientation (IO) parameters of the HiRIC, the camera was calibrated in the laboratory before

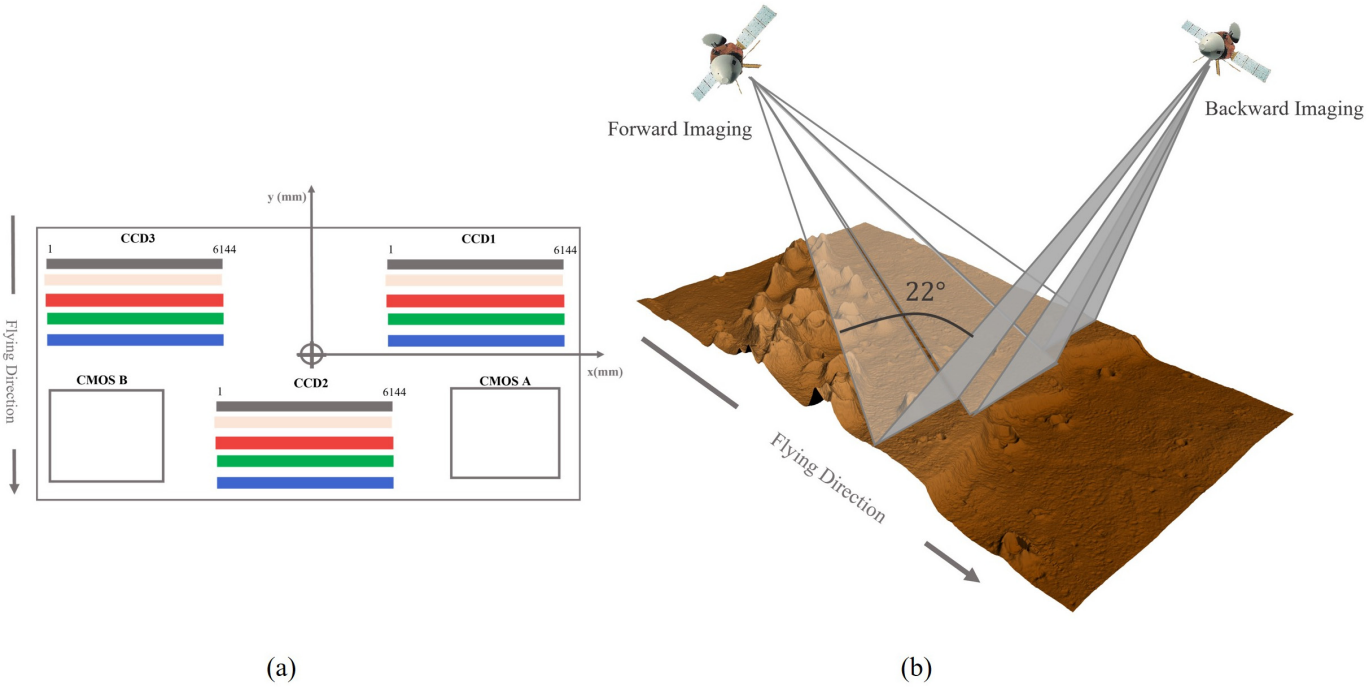

Fig. 2. Imaging principle of HiRIC. (a) HiRIC focal plane layout. (b) Cross-orbit stereo configuration of HiRIC images.

TABLE I
PARAMETERS OF THE HiRIC

Parameters	HiRIC
Focal length	4,640 mm
Active pixels per CCD line	6144
Pixel size	8.75 μm
Spatial resolution	0.5 m/pixel @ 265 km
Swath per orbit	9 km @ 265 km
Spectral filters	one panchromatic, four color
Panchromatic	0.45–0.9 nm
Blue (BL)	0.45–0.52 nm
Green (GR)	0.52–0.60 nm
Red (RE)	0.63–0.69 nm
Near-infrared (IR)	0.76–0.9 nm

launch. The calibration precision for the focal length, principal point offset, and lens distortion is better than 0.05%, 0.002 mm, and 0.3%, respectively [8]. The transformation between the image coordinate (s_{ccd}, l_{ccd}) and the focal plane coordinate (x, y) can be defined as

$$\begin{bmatrix} x \\ y \end{bmatrix} = T_n \times \boldsymbol{p} = \begin{bmatrix} a_{11} & a_{12} & a_{13} \\ a_{21} & a_{22} & a_{23} \end{bmatrix}_n \begin{bmatrix} s_{\text{ccd}} \\ l_{\text{ccd}} \\ 1 \end{bmatrix} (n = 1, 2, 3) \quad (1)$$

where $T_n = \begin{bmatrix} a_{11} & a_{12} & a_{13} \\ a_{21} & a_{22} & a_{23} \end{bmatrix}_n$ is a set of affine transformation parameters. Parameters a_{13} and a_{23} contain translations from the principal point. Parameters a_{11} to a_{22} model pixel dimensions and the rotation component. Assuming that the rotation angle between the image coordinate and the focal plane coordinate is θ, these parameters can be calculated as follows:

$$\begin{cases} a_{11} = -\cos\theta * k \\ a_{12} = \sin\theta * k \\ a_{13} = (S_{\text{ccd}} - S_{\text{mid}}) * \cos\theta * k \\ a_{21} = \sin\theta * k \\ a_{22} = \cos\theta * k \\ a_{23} = Y_{\text{ccd}} - (S_{\text{ccd}} - S_{\text{mid}}) * \sin\theta * k \end{cases} \quad (2)$$

where k is the pixel dimension, S_{ccd} is the sample number from the starting of each CCD array, S_{mid} is the sample number at the center of CCD2, and Y is the offset of the CCD array along the flying direction in millimeters.

The EO parameters of the HiRIC images differ for each image line. The mission control center provides the HiRIC position and pointing information in the J2000 coordinate system at intervals of 30 s and 2 s, respectively. Spline interpolation of the position and pointing data is verified to be accurate enough to recover the nominal EO parameters for each image line. With the transformation matrix P_{J2000}^{Mars} acquired from the corresponding ephemeris data, the nominal EO parameters P_{J2000} can be converted to the Mars body-fixed coordinate frame P_{Mars} using (3). The linewise EO data are fit by second-order polynomial coefficients $a_1 - f_3$ to describe the position (X_t, Y_t, Z_t) and pointing $(\varphi_t, \omega_t, \kappa_t)$ parameters

of the HiRIC images at time t using (4)

$$P_{\text{Mars}} = P_{J2000}^{\text{Mars}} \times P_{J2000} \tag{3}$$

$$\begin{cases} X_t = a_1 + a_2 t + a_3 t^2 \\ Y_t = b_1 + b_2 t + b_3 t^2 \\ Z_t = c_1 + c_2 t + c_3 t^2 \\ \varphi_t = d_1 + d_2 t + d_3 t^2 \\ \omega_t = e_1 + e_2 t + e_3 t^2 \\ \kappa_t = f_1 + f_2 t + f_3 t^2. \end{cases} \tag{4}$$

Next, RPC fitting [22] is conducted based on the second-order polynomials. With the known highest and lowest elevation in the corresponding region, the 3-D space is segmented into multiple layers to provide abundant virtual ground control points. The corresponding points in the image space are then calculated via the second-order polynomial model described above. Finally, the calculation of the RPCs can be formulated as a mathematical optimization problem [28].

Even though the direct use of IO and EO parameters is intuitive, RPC fitting is introduced here for the following reasons: 1) RPCs do not depend on a specific trajectory model, providing more flexibility to improve the mathematical geometry without modifying the subsequent procedures; 2) the generated RPCs can be used in commercial photogrammetry or image analysis software (e.g., LPS, ArcGIS, and ENVI), leading to more convenient 3-D and 2-D analysis; 3) once the RPCs are fit, the time-consuming iterative projection and backprojection procedures for determining the 2-D and 3-D correspondences of pushbroom images can be omitted [28] to achieve high-efficiency processing; and 4) RPC-based bundle adjustment could absorb other possible errors in the camera intrinsic parameters [22], leading to similar performances as considering self-calibration in bundle adjustment but offering more simplicity.

C. Deep-Learning-Based Tie-Point Matching

Tie-point matching comprises two separate steps: matching within the narrow overlapping region between the adjacent CCD images and matching in the overlapping images from multiple orbits. The first step aims to connect the three CCD images in a single orbit, and the second step focuses on connecting the stereo images from multiple orbits.

For tie-point matching between the adjacent CCD images, very few feature points can be matched within the narrow overlapping region of ~140 pixels using conventional methods, such as SIFT [15]. The SIFT algorithm fails to detect sufficient feature points, which is further exacerbated by the subsequent homography-based filtering process. Insufficient tie points will lead to difficulties in preserving the consistency between CCD images, introducing apparent artifacts in the resulting DEM products.

To achieve robust and sufficient tie-point matching results, we use state-of-the-art deep-learning-based algorithms, Superpoint and SuperGlue [9], [29], for image matching. Superpoint is for feature point extraction, and SuperGlue is used together with Superpoint for feature point matching [18]. Unlike SIFT-like detectors, Superpoint features are trained using basic shapes (e.g., triangles, cubes, checkerboards, and stars) and have succeeded in extracting abundant features in narrow image regions (e.g., corners of sand dunes and crater rims). Furthermore, the matching algorithm SuperGlue combines the merits of self- and across-attention natural language processing [30] to describe the relationships between the features within an image and across images to be matched based on graph theory. Because the deep-learning-based algorithms are mainly computed on GPUs, exploiting the RPCs of images to restrict matching in the roughly overlapping region of images can boost efficiency and accuracy. Specifically, in our practice, the long HiRIC images are segmented into small subsets (8000 pixels in length suggested in this article) covering the same latitude range and fed into the Superpoint and SuperGlue pipeline pair by pair.

Fig. 3(a) shows the tie-point matching results obtained using the Superpoint and SuperGlue algorithms and a comparison with the results obtained using SIFT. The blue points present the extracted feature points, while the red lines show the successful matches. It is obvious that SIFT fails in obtaining sufficient tentative feature points, and most of them tend to be clustered in local regions with distinct textures. It is difficult for SIFT to obtain sufficient successful matches in the narrow overlapping region of the adjacent CCD images, as only several matches can be noticed in the right panel of Fig. 3(a). SuperGlue, on the other hand, successfully detects a large number of feature points and matches sufficient tie points within the narrow overlapping region of the adjacent CCD images. Fig. 3(b) shows examples of matched tie points by SuperGlue in the overlapping images from different orbits. Because the overlapping region varies in each stereo pair for images from multiple orbits, overlap detection is first conducted to identify image pairs for the following matching module to avoid redundant computation. After pairwisely matching the tie points using Superpoint and SuperGlue, the same tie points matched among different image pairs are linked by the connected component algorithm [31] to form a longer feature track for stable bundle adjustment.

D. Bundle Adjustment of Multi-CCD Images

Bundle adjustment based on RPCs can be accomplished by modeling the difference $(\Delta x, \Delta y)$ in the image space between the observations (x, y) and the reference or ground truth $(\hat{x}, \hat{y})$, as shown in the following equation:

$$\begin{aligned} \Delta x &= \hat{x} - x = \hat{x} - \big(a_0 + a_S * \text{Sample} + a_L * \text{Line} \\ &\quad + a_{\text{SL}} * \text{Sample} * \text{Line} + a_{S2} * \text{Sample}^2 + a_{L2} * \text{Line}^2\big) \\ \Delta y &= \hat{y} - y = \hat{y} - \big(b_0 + b_S * \text{Sample} + b_L * \text{Line} \\ &\quad + b_{\text{SL}} * \text{Sample} * \text{Line} + b_{S2} * \text{Sample}^2 + b_{L2} * \text{Line}^2\big) \end{aligned} \tag{5}$$

where $\{a_0 \dots b_{L2}\} \in \boldsymbol{A} \in \mathbb{R}^{2\times 6}$ are the adjustable parameters, and Sample and Line represent the image coordinates inferred from the object coordinates. It is worth noting that the HiRIC images have lengths of more than 240 000 lines, several times longer than other Mars orbital images (i.e., CTX, HiRISE, and HRSC). The conventional affine correction strategy, which

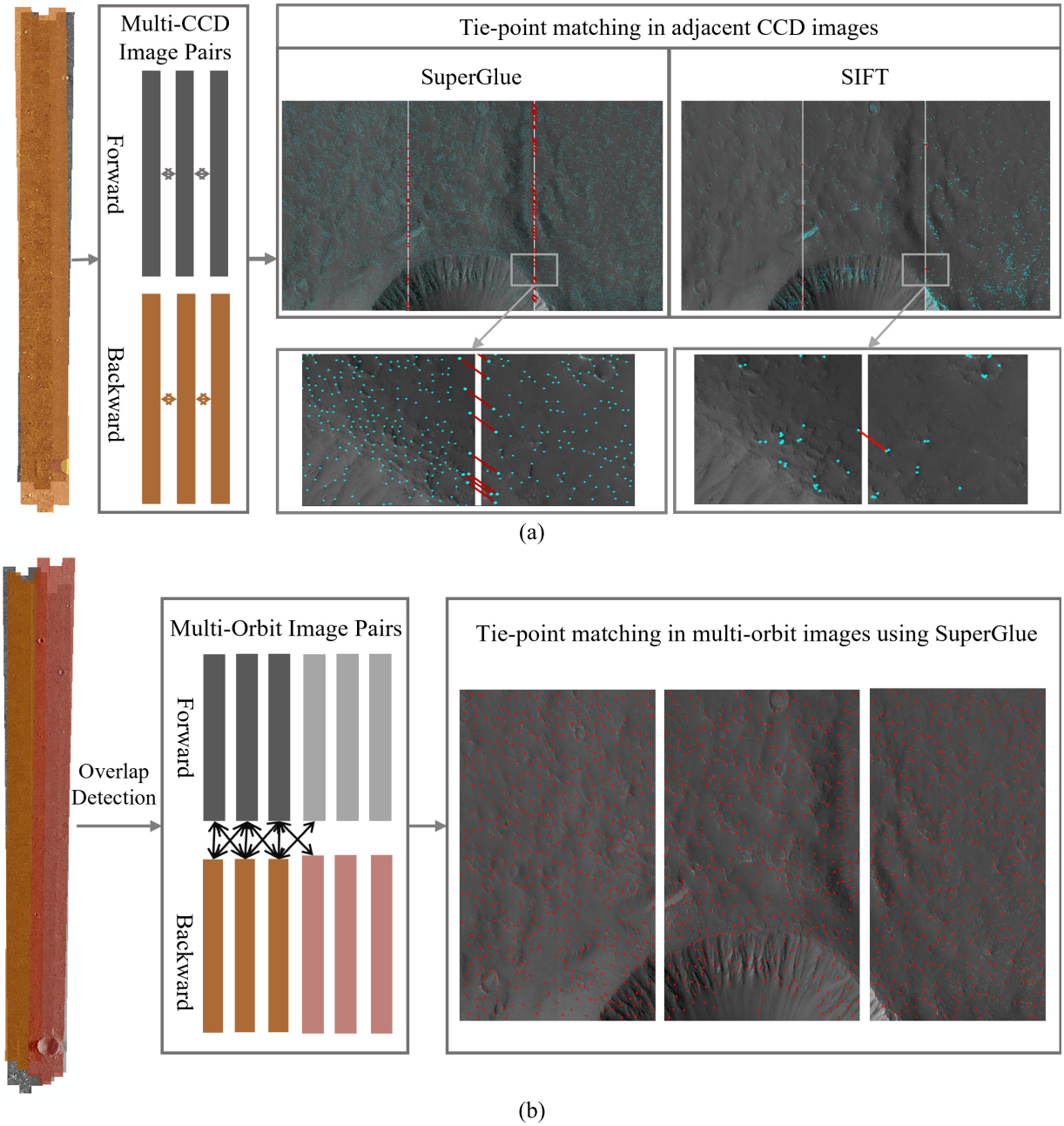

Fig. 3. Tie-point matching in the HiRIC images. (a) Matching in multi-CCD images. (b) matching in multi-orbit images.

limits the adjustable parameters to the first order [22], may not be sufficient to describe the geometry of the HiRIC images. Therefore, we use bundle adjustment based on the second-order formula, as shown in (5), with 12 adjustable parameters in this study

$$\begin{cases} v_{\text{projection-inner}} \\ = w_{\text{inner}}\left(\boldsymbol{x}_{ij} - \boldsymbol{A}_j \Pi(\boldsymbol{X}_i)\right), & \boldsymbol{x}_{ij} \text{for inner-orbit tiepoints} \\ v_{\text{projection-cross}} \\ = w_{\text{cross}}\left(\boldsymbol{x}_{ij} - \boldsymbol{A}_j \Pi(\boldsymbol{X}_i)\right), & \boldsymbol{x}_{ij} \text{for cross-orbit tiepoints} \\ v_{\text{control}} = w_{\text{control}}\left(h_i - \hat{h}_i\right) \\ v_{\text{observation}} = w_A\left(\boldsymbol{A}_j - \boldsymbol{I}\right) \end{cases} \tag{6}$$

$$w = \sqrt{\lambda} / \left(\sqrt{N} \times \sigma\right). \tag{7}$$

Equation (6) shows the three types of cost functions forming the optimization problem in bundle adjustment, namely, projection constraint, control constraint, and observation constraint. The projection constraint aims to force the ith tie point on the jth image $\boldsymbol{x}_{ij}$ to be intersected at a certain 3-D point $\boldsymbol{X}_i$ in the object space. w_{inner} and w_{cross} refer to the normalized weights of the inner orbit and cross-orbit tie points, respectively, and can be calculated based on predefined weight λ, prior precision σ, and the normalization factor N using (7) [28]. This formulation explicitly states that the type with fewer tie points is expected to have a higher weight, which will balance the weights of the above two types of tie points in the bundle adjustment process to simultaneously achieve inner orbit and cross-orbit consistency. The second type of cost function serves to guarantee that the calculated

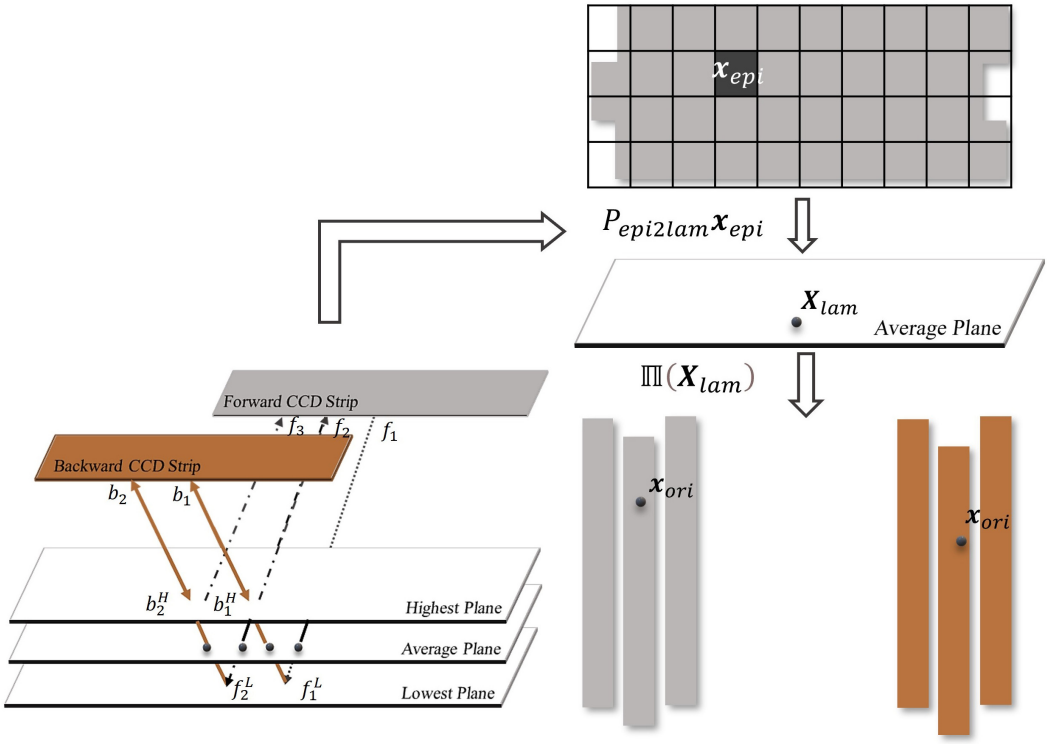

Fig. 4. Illustration of the tripled-epipolar rectification. (a) Retrieval of the dominant epipolar direction. (b) Two main steps involved in the procedure.

elevation h_i is consistent with the reference datum $\hat{h_i}$ (e.g., MOLA). While these cost functions tackle the aforementioned inconsistencies, the third type of function is indispensable to constrain the fluctuation of $\boldsymbol{A}_j$, the matrix of the unknown parameters in (5), which is assigned an initial value of $\begin{bmatrix} 0 & 1 & 0 & 0 & 0 \\ 0 & 0 & 1 & 0 & 0 \end{bmatrix}$. During each iteration in the bundle adjustment process, residuals for each tie point are calculated. Those that exceed three times the mean square error are considered outliers, and the projection and corresponding control constraint of the outliers are omitted in the next iteration [32].

Once the adjustable parameters $\boldsymbol{A}_j$ are calculated, they are integrated into the RPCs through a refitting process. The process is similar to that described previously, except the projection relationship changes from the polynomial-based collinearity function to the RPC-based function $x = \boldsymbol{A}_j \Pi(\boldsymbol{X}_i)$. The reverse RPCs projecting the image coordinates to the 3-D object coordinates are also calculated based on the bundle adjustment results.

E. Tripled-Epipolar Image Generation From Multi-CCD Images

Transforming the individual CCD images into the epipolar space not only eliminates the vertical disparities to dramatically improve the dense image matching efficiency and accuracy but also enables the generation of a merged epipolar image to maintain internal consistency. As shown in Fig. 4(a), a well-established algorithm [33] for pushbroom camera epipolar geometry is utilized and extended for tripled-epipolar image generation of the HiRIC images.

The epipolar rectification establishes an affine transformation P_{epi2lam} between the epipolar image space and the Lambert plane (see Fig. 4). The first step is to determine the dominant epipolar direction. As shown in Fig. 4(a), a point f_1 on the forward CCD strip can be projected to f_1^L on the lowest plane and further backprojected to b_1 on the backward CCD strip. b_1 can be subsequently projected to b_1^H on the highest plane and further backprojected to f_2 on the forward CCD strip. This process can be repeated to retrieve sufficient image points to form a half of the epipolar line. The other half can be obtained by projecting f_1 to the highest plane first and repeating the above procedure. These points are then transferred into the Lambert plane to fit a straight line with a direction defined as the dominant direction of the epipolar image, which can be used to determine the rotation component R_{epi2lam} of the affine transformation P_{epi2lam}.

With the given ground sampling distance S_{epi} and the calculable translation component T_{epi}, the affine transformation P_{epi2lam} between a pixel on the epipolar image $\boldsymbol{x}_{\text{epi}}$ and its corresponding location $\boldsymbol{X}_{\text{lam}}$ on the Lambert plane can be formulated, as shown in (8). $\Pi(\boldsymbol{X}_{\text{lam}})$ in (8) refers to the backprojection of $\boldsymbol{X}_{\text{lam}}$ on the Lambert plane to the pixel coordinates in the original forward and backward CCD images [see Fig. 4(b)] based on their RPCs

$$\begin{aligned} \boldsymbol{x}_{\text{ori}} &= \Pi(\boldsymbol{X}_{\text{lam}}) \\ \boldsymbol{X}_{\text{lam}} &= P_{\text{epi2lam}}\boldsymbol{x}_{\text{epi}} = S_{\text{epi}}[R_{\text{epi2lam}}|T_{\text{epi}}]\boldsymbol{x}_{\text{epi}}. \end{aligned} \tag{8}$$

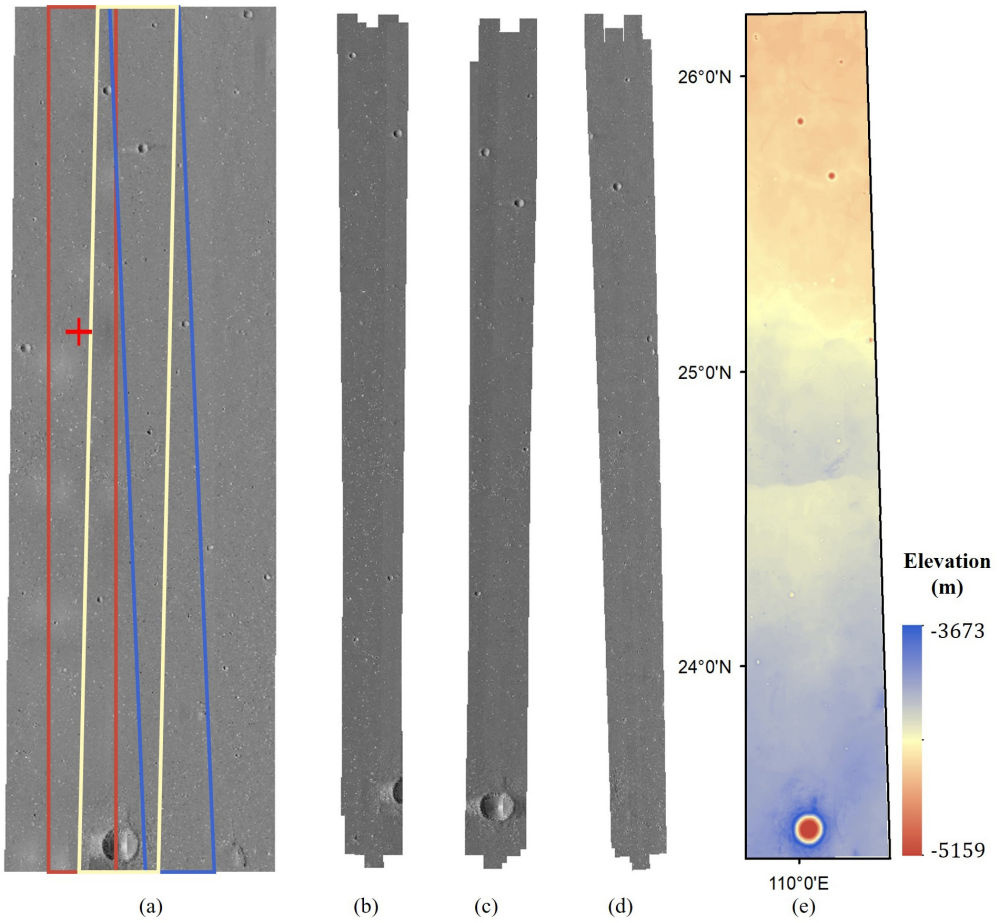

Fig. 5. HiRIC images used for the experimental analysis. (a) HiRIC image coverage overlaid on an HiRIC image mosaic covering the Zhurong landing region. The Zhurong landing site is marked by the red cross; (b)–(d) separate pairs of HiRIC images with orbit numbers 0324-0326, 0316-0318, and 0306-0308, corresponding to the red, yellow, and blue boxes marked in (a). (e) DEM (3.5 m/pixel) generated from the HiRIC images.

The above procedure can yield a pair of epipolar images. However, the layout of the three CCDs impedes them from being processed as one image, and treating each CCD as a single image may involve more complex steps to register and fuse the multiple disparity maps. Thus, a tripled-epipolar rectification algorithm based on our previous method [17] is developed to merge the three CCD images in epipolar space. Although the epipolar lines of the pushbroom satellite images are in a hyperbola format, Wang *et al.* [33] showed that they can be regarded as parallel. The epipolar lines of the three CCD images should also be parallel within the same orbit. Thereby, the above dominant direction retrieval algorithm is repeatedly performed on the three CCD pairs, and their average direction is used for tripled-epipolar image generation.

F. Block Adjustment of Multi-orbit Images

While the bundle adjustment of multi-CCD images handles the internal consistency and accuracy within a stereo pair of HiRIC images, the block adjustment improves the consistency and accuracy of multi-orbit HiRIC images. Based on the previously derived cross-orbit tie points, one orbit with good planimetric accuracy is regarded as the reference, sequentially propagating its position information to neighboring orbits through block adjustment. The constraints are the same as the bundle adjustment constraints. With a high prior precision σ_{rot}, the modification of the RPCs of an orbit can be approximated as a pure translation transformation. Therefore, the translation part in P_{epi2lam} should be modified accordingly to P'_{epi2lam} for the following space intersection use.

It should be noted that no ground control points are involved in both the bundle adjustment and block adjustment processes. A number of reference points extracted from a CTX image mosaic [3] covering the study area are used to adjust the planimetric positions of the HiRIC images during the RPC generation. In the subsequent bundle/block adjustment, the MOLA DEM is regarded as the reference datum so that the space intersection of the tie points coincides with the MOLA elevations in local areas.

G. Dense Image Matching and DEM Generation

Dense image matching to retrieve the disparity for each pixel is then performed using the tripled-epipolar images. The process is separated into: 1) disparity retrieval and 2) subpixel refinement. SGM [23], which casts the global optimization problem into dynamic programming in eight or more directions, is a widely used algorithm for efficiently retrieving

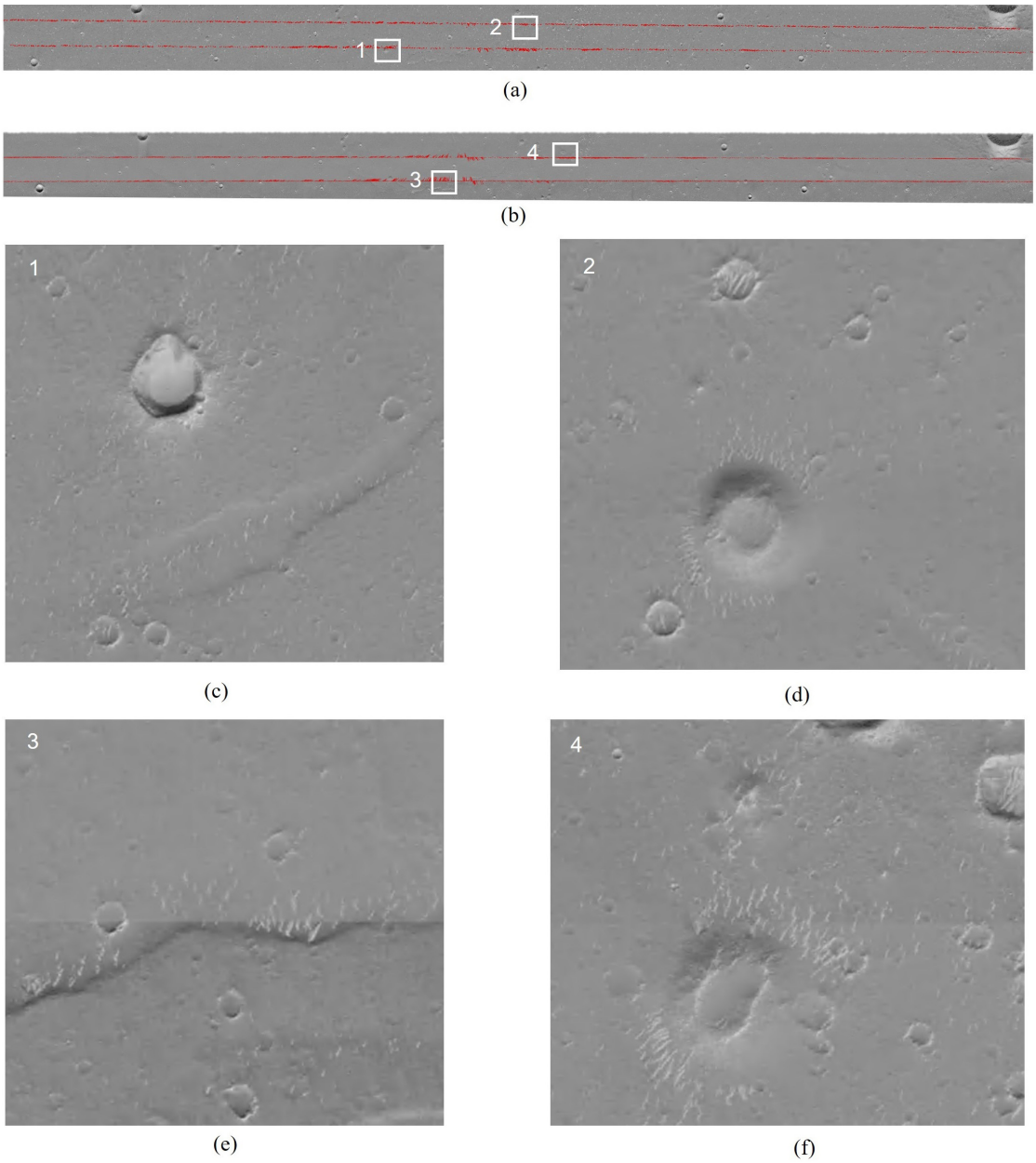

Fig. 6. Evaluation of the bundle adjustment of multi-CCD images. (a)–(b) Error vectors (exaggerated 100 times) in epipolar space for orbits 0324 and 0326. (c)–(f) Representative enlarged views showing the mosaicking of adjacent CCD images.

the disparity. The large computational volume involved in the reconstruction of planetary images can be parallelly processed by separating the long image strip into several tiles (8000 image lines in this research) and fusing them together after the cross-check. However, as the energy function implicitly assumes that the adjacent disparities should be close, it oversmooths the local region and fails to recover the discontinuities and subtle textures. Therefore, LSM [34] is implemented to refine the disparities into subpixel accuracy.

Knowing the disparities between the epipolar images, their pixelwise correspondence is obtained and passed to the original images using P'_{epi2lam}. Space intersection is then conducted to calculate the 3-D coordinates of the matching points based on the refined RPCs after bundle adjustment and block adjustment. The 3-D point clouds are then interpolated to generate DEMs as the topographic mapping product. Orthoimages are also generated from the DEMs and refined RPCs.

IV. Experimental Evaluation Using HiRIC Images of the Zhurong Landing Region

A. Dataset Description

Since the Tianwen-1 probe entered the Mars orbit in February 2021, intensive studies of the candidate landing site in southern Utopia Planitia have been conducted using data from the HiRIC and other sensors [3]. With an approximately 300-km orbit height, the HiRIC image resolution can reach 0.7 m/pixel, which allows high-resolution mapping to reveal the detailed topography. Three stereo pairs of HiRIC images of the Zhurong landing region are selected

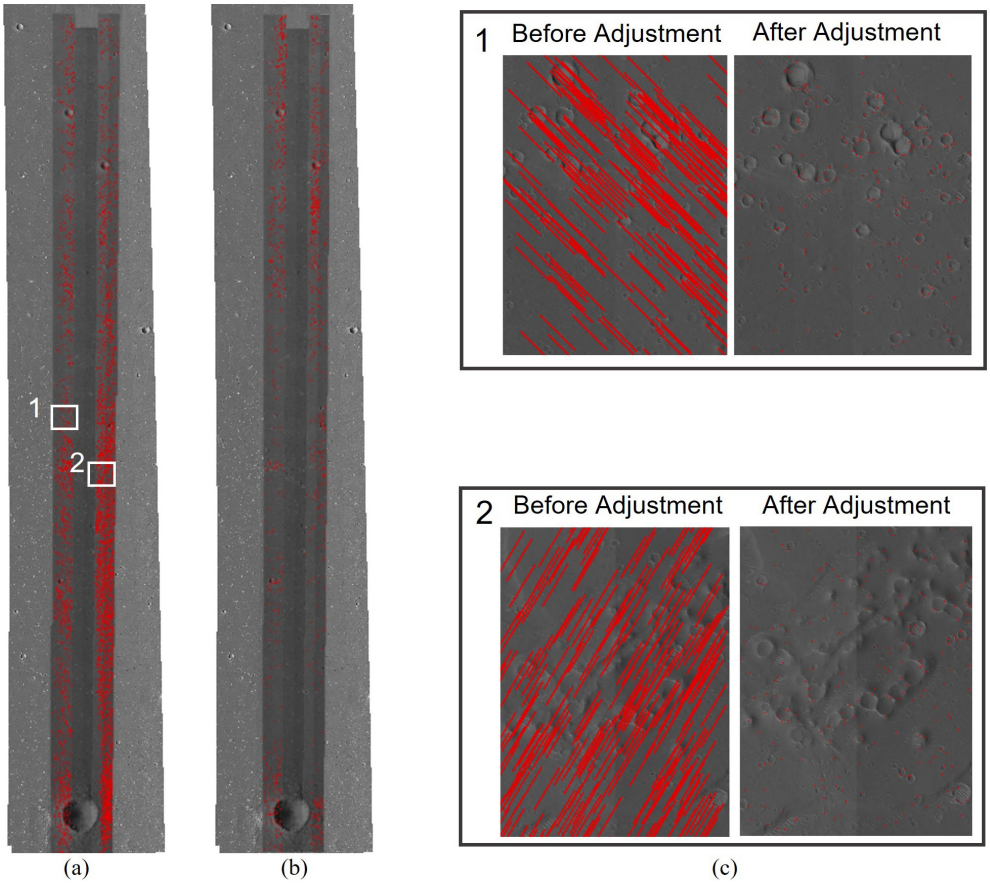

Fig. 7. (a) and (b) Error vectors illustrating image residuals before and after block adjustment (exaggerated 40 times). (c) Zoomed-in view of the boxes marked in (a).

TABLE II
INFORMATION ON THE HiRIC IMAGES USED FOR THE EXPERIMENTAL ANALYSIS

Orbit No.	Acquisition Date	Image Length (pixels)	Center Latitude and Longitude
0306	06/03/2021	241,000	24.744°, 110.169°
0308	08/03/2021	264,000	24.745°, 110.157°
0316	16/03/2021	253,000	24.715°, 110.033°
0318	18/03/2021	280,000	24.782°, 110.039°
0324	24/03/2021	254,000	24.784°, 109.891°
0326	26/03/2021	280,000	24.730°, 109.879°

for experimental analysis, as shown in Fig. 5. The forward- and backward-looking images of the first orbit (marked by the red box) covering the Zhurong landing site [red cross in Fig. 5(a)] were acquired on March 24 and 26, 2021, with more than 18 000 × 250 000 pixels for each image. The second and third stereo pairs have a length of up to 260 000 pixels, covering the eastern region of the first stereo pair. The detailed information for the three stereo pairs of HiRIC images is listed in Table II. Owing to the clear weather during these days, the HiRIC images are of satisfactory quality (e.g., favorable signal-to-noise ratio and consistent illumination). Therefore, a DEM with a resolution of 3.5 m/pixel (five times the image resolution) is generated using the photogrammetric method, as shown in Fig. 5(e).

To evaluate the performance of the proposed photogrammetric method, the geometric accuracy and reconstruction details of the HiRIC DEM are compared with reference DEMs generated from the MOLA data and HiRISE images. The MOLA DEM provides the most accurate Martian topography reference data [10], [35]. Several HiRISE images with resolutions of 0.25 m/pixel are available within the Zhurong landing region, and DEMs with a resolution of 1 m/pixel are generated by photogrammetric processing [7], [11].

B. Evaluation of the Bundle Adjustment of Multi-CCD Images

The bundle adjustment of multi-CCD images is evaluated in the epipolar space for intuitive analysis. Fig. 6 and Table III present the projection error of each tie point in the epipolar

TABLE III
STATISTICS OF THE IMAGE RESIDUALS AFTER MULTI-CCD BUNDLE ADJUSTMENT FOR ORBITS 0324 AND 0326

	No. of tie points	Horizontal (pixels)			Vertical (pixels)		
		Mean	Maximum	RMSE	Mean	Maximum	RMSE
1. Orbit 0324 (forward)							
CCD1-2	3036	0.26	0.73	0.25	0.24	0.71	0.23
CCD2-3	1948	0.34	0.62	0.69	0.66	0.95	0.82
2. Orbit 0326 (backward)							
CCD1-2	3340	0.32	0.78	0.37	0.36	0.93	0.43
CCD2-3	1560	0.33	0.89	0.28	0.31	0.66	0.29

TABLE IV
STATISTICS OF IMAGE RESIDUALS OF THE BLOCK ADJUSTMENT OF MULTI-ORBIT HiRIC IMAGES

		Image Residuals (pixels)		
		Mean	Maximum	RMSE
Orbit 0306-08 and Orbit 0316-18				
Before BA	*X*	1.72	15.89	1.04
	Y	2.38	17.85	1.37
	2D	3.02	19.84	1.86
After BA	*X*	0.15	0.55	0.12
	Y	0.18	0.51	0.14
	2D	0.24	0.61	0.21
Orbit 0324-26 and Orbit 0316-18				
Before BA	*X*	3.02	24.92	1.42
	Y	4.06	27.59	1.89
	2D	6.12	27.90	3.30
After BA	*X*	0.22	0.79	0.14
	Y	0.28	0.83	0.18
	2D	0.43	0.85	0.44

space for orbits 0324 and 0326, which explicitly assumes that the tie points are projected to the same position in epipolar space, with residuals indicating the bundle adjustment performance. Three statistical indexes [i.e., the maximum, mean, and root mean square error (RMSE)] of the image residuals along the horizontal and vertical directions are also calculated, as shown in Table III. It is evident that the tie points are distributed evenly throughout the orbit, and the projection error is small even when exaggerated 100 times [see Fig. 6(a) and (b)]. The inconsistency among adjacent CCD images after bundle adjustment is considered negligible because the calculated projection residuals are all less than one pixel, leading to well-fused tripled-epipolar images without apparent displacement between the adjacent CCD images [see the enlarged views of the epipolar images in Fig. 6(c) and (d)]. It should be noted that the number of tie points between CCD1 and CCD2 images is greater than that between CCD2 and CCD3. This is because CCD3 is more blurred than the other two CCDs, which takes a toll on the matching of CCD2-3, leading to fewer tie points than CCD1-2. However,

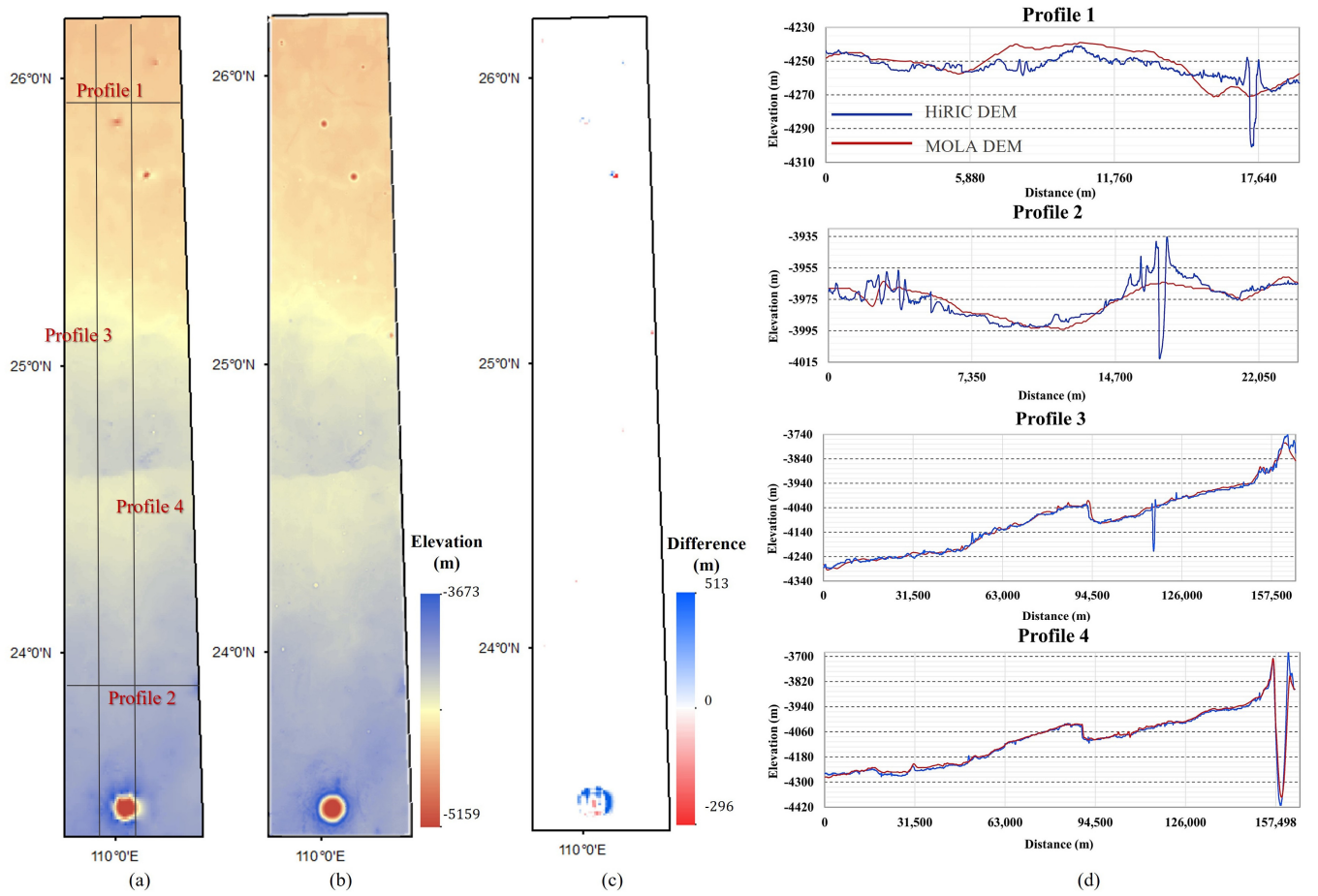

Fig. 8. Accuracy analysis of the generated HiRIC DEM. (a) Corresponding MOLA DEM (463 m/pixel). (b) Generated HiRIC DEM (3.5 m/pixel). (c) Difference map between the HiRIC DEM and MOLA DEM. (d) Elevation profiles of the lines marked in (a).

this discrepancy does not result in unbalanced bundle adjustment results, and the consistency between both CCD pairs is properly maintained.

C. Evaluation of the Block Adjustment of Multi-orbit Images

Fig. 7 and Table IV show the results of the block adjustment of the three stereo orbits covering the Zhurong landing region. Beginning with the adjusted RPCs derived from the single stereo orbit adjustment, the block adjustment eliminates inconsistencies among different orbits of images. In the experiment, orbit 0324-26 in the westernmost is treated as the reference to sequentially adjust the other two orbits. As shown in Fig. 7(b), the backprojection error in the image space among the orbits dramatically decreases from dozens of pixels in maximum to subpixel, demonstrating the effectiveness of the block adjustment. This improvement is visualized in the zoomed-in view in Fig. 7(c), where long error vectors are shortened to small points after the adjustment. As no ground control point measured from MOLA is leveraged in the block adjustment to register the HiRIC orbit strictly, the process is still a free network block adjustment.

D. Evaluation of the Generated DEM

Fig. 8 presents a side-by-side comparison of the generated HiRIC DEM and the MOLA DEM, revealing an overall smooth slope down to the north and providing a suitable place for rover landing [3]. The 3-D information of distinct landforms (i.e., the large craters, a series of dunes, and ridges) is properly reconstructed. Verified by the corresponding MOLA DEM in Fig. 8(a) and the difference maps in Fig. 8(c), the global trend of the HiRIC DEM agrees well with the reference MOLA DEM. Apart from the overall difference map, the four profiles marked in Fig. 8(a) are also analyzed quantitatively in Fig. 8(d). Three statistical indexes (i.e., the maximum, mean,

TABLE V
STATISTICS OF THE COMPARISON BETWEEN THE HiRIC AND MOLA DEMs

	Absolute Elevation Differences (m)		
	Mean (95th percentile)	Maximum (95th percentile)	RMSE (95th percentile)
Profile 1	5.39 (4.71)	30.15 (14.05)	4.52 (3.33)
Profile 2	4.69 (3.72)	47.67 (12.72)	5.64 (2.94)
Profile 3	8.28 (6.32)	180.73 (20.72)	12.44 (4.32)
Profile 4	9.92 (6.84)	224.74 (20.65)	18.21 (4.44)
Difference Map	8.69 (6.10)	513.21 (20.75)	19.77 (4.45)

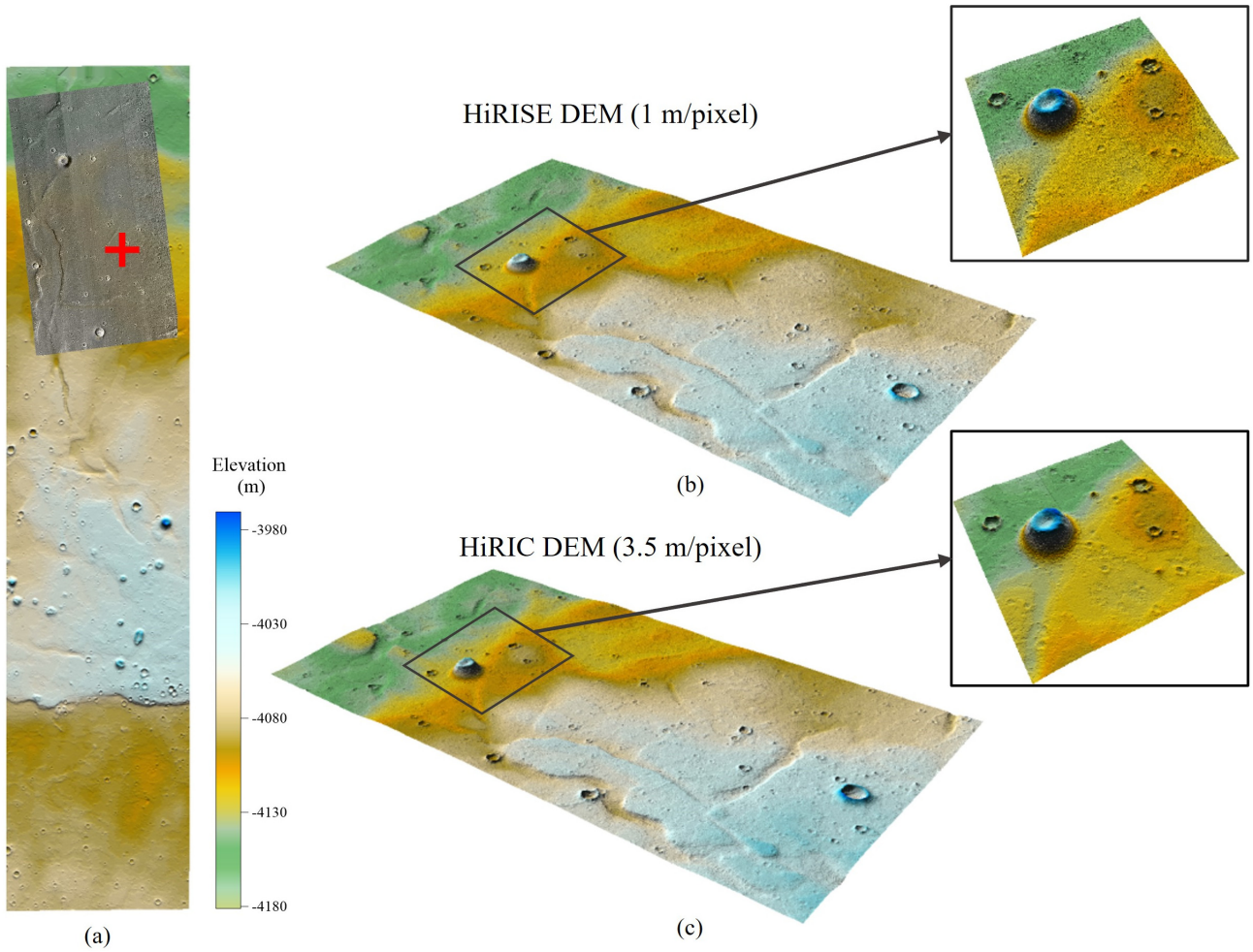

Fig. 9. 3-D views of the HiRIC and HiRISE DEMs at the Zhurong landing region. (a) HiRIC DEM covering the Zhurong landing site with the HiRISE images overlaid, and the Zhurong landing site is marked by the red cross. (b) 3-D view of the HiRISE DEM (1 m/pixel) used for comparison. (c) 3-D view of the HiRIC DEM (3.5 m/pixel) cropped to the same area of the HiRISE DEM.

and RMSE) of the profiles and the DEMs are calculated, as listed in Table V. As the elevation discrepancies hardly follow the normal distribution, the 95th percentile errors are also presented in Table V. Results show that, after excluding the gross errors, both the 95th percentile mean deviation and RMSE are less than 7 m, indicating the favorable performance of the developed photogrammetric workflow. The gross errors are mainly happened around the large crater closed to the south boundary of the study area, where the MOLA DEM omitted the right-hand side of the crater, while the HiRIC DEM successfully reconstructed the entire crater. Profile 4 in Fig. 8(d) indicates a deviation as large as about 220 m between the two DEMs in the crater region. However, the overall deviation is still within a reasonable range [16]. In addition, the more than 100-fold resolution difference results in some detailed textures (i.e., small craters, cones, and troughs) being recovered by the HiRIC DEM but missed by MOLA. The subtle misalignment between the two DEMs may exacerbate this difference.

To examine the details of the generated HiRIC DEM, a local region surrounding the Zhurong landing site is selected and compared with the 1 m/pixel HiRISE DEM. The region shown in Fig. 9 is a subset of the 0324-26 orbit, where the Zhurong landing location is indicated by the red cross.

As shown in Fig. 9(a), this region features a series of troughs, craters, and cones, despite the overall flat trend. These landforms may provide evidence for the eruption of muddy debris [36], offering an appropriate landing site in terms of both landing safety and scientific significance. This subset region contains more than 18 000 × 40 000 pixels across the three CCD images. Within this relatively small area, the overlapping region for adjacent CCDs from stereo pairs is approximately a rectangle more than 1000 pixels wide. As illustrated in Fig. 9(b) and (c), the 3-D view of the HiRISE DEM and the HiRIC DEM is visually similar; however, the HiRIC DEM is inevitably smoothed due to the original image resolution. Facilitated by subpixel LSM, all the distinctive landforms captured by the HiRIC images are well-reconstructed with sufficient detail (i.e., the sand dunes inside the troughs) and precise elevation.

To quantitatively study the geometrical accuracy, two profiles are drawn vertically and horizontally through the entire region [see Fig. 10(a)] for comparison of the HiRIC and HiRISE DEMs, and results are shown in Fig. 10(c). Fig. 10(b)

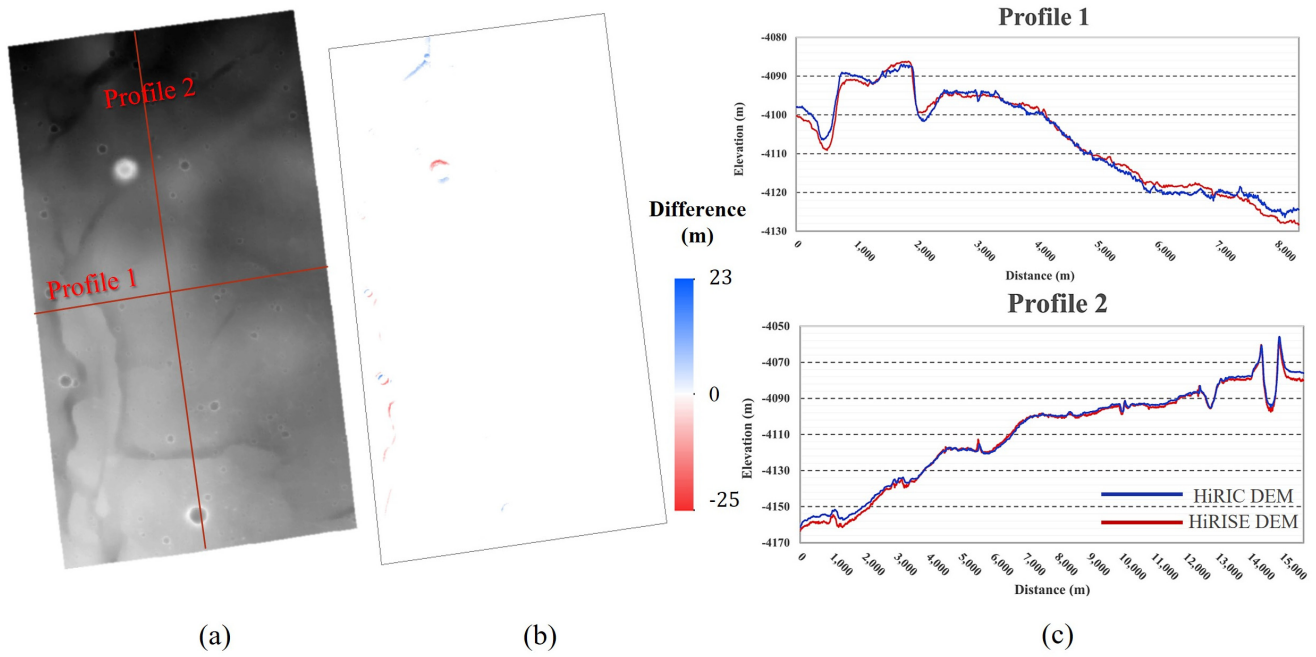

Fig. 10. Comparison between the HiRIC and the HiRISE DEMs. (a) Profiles shown on the HiRISE DEM for reference. (b) Difference map between the HiRISE and HiRIC DEMs. (c) Comparison of the profiles marked in (a).

TABLE VI
STATISTICS OF THE COMPARISON BETWEEN THE HiRIC AND HiRISE DEMS

	Absolute Elevation Differences (m)		
	Mean (95th percentile)	Maximum (95th percentile)	RMSE (95th percentile)
Profile 1	1.27 (1.15)	5.03 (2.87)	0.94 (0.79)
Profile 2	1.45 (1.29)	7.54 (3.98)	1.23 (1.03)
Difference map	2.08 (1.80)	25.25 (5.31)	1.86 (1.31)

also shows a direct difference map of the two DEMs. Fig. 10(b) and (c) shows a good level of consistency between the HiRIC DEM and the HiRISE DEM, with only 2.08-m mean error and 1.86-m RMSE, as listed in Table VI. Because the 1-m/pixel HiRISE DEM is considered the ground truth of the region, the difference between the two DEMs is the most likely source of error, rather than a simple deviation. The maximum error occurs in the border region with the large cone and crater, owing to the slightly deviated elevation.

V. CONCLUSION AND DISCUSSION

This article presents a novel photogrammetric method for Mars topographic mapping using the HiRIC images. Through the multi-CCD bundle adjustment and tripled-epipolar rectification, the multi-CCD residuals in one orbit are constrained to less than one pixel in the epipolar space. Consistency among multiple-orbits is then achieved via multi-orbit block adjustment, resulting in subpixel image residuals. The 3-D accuracy of the generated DEM is also evaluated, showing a mean deviation (95th percentile) of 6.1 m compared with the MOLA DEM and 1.8 m compared with the HiRISE DEM. The generated HiRIC DEM also shows subtle topographic details compared to the HiRISE DEM. The results demonstrated the promising performance of the proposed method.

Limited by the currently available HiRIC data, the universality of the proposed methodology requires further investigation and some steps may be adapted to address newly arising issues. However, as the photogrammetric workflow is developed based on RPCs, the adaptions could be conveniently embedded. In addition, some details captured by the images still fail to be reconstructed properly, mainly due to the approximate epipolar image generation and the effect of noise on the matching cost in the SGM stage. Therefore, a more robust matching cost instead of a census should be implemented to capture higher level features and adapt to different illumination conditions. Moreover, photoclinometric methods [12] are expected to compensate for the missing textures and improve the retrieval of topographic details.

As the second-highest resolution imaging sensor orbiting Mars, the HiRIC could complement the existing submeter datasets of the Martian surface. The success of topographic mapping based on the HiRIC images offers the possibility of global high-precision (3.5 m/pixel) topographic mapping of Mars, facilitating future exploration missions and Mars scientific research.

ACKNOWLEDGMENT

The authors would like to thank all those who worked on the archive of the datasets to make them publicly available and the anonymous reviewers who provided valuable comments and suggestions.

REFERENCES

[1] J. Liu *et al.*, "Geomorphic contexts and science focus of the Zhurong landing site on Mars," *Nature Astron.*, vol. 6, no. 1, pp. 65–71, Jan. 2022, doi: 10.1038/s41550-021-01519-5.

[2] B. Wu *et al.*, "Characterization of the candidate landing region for Tianwen-1—China's first mission to Mars," *Earth Space Sci.*, vol. 8, no. 6, Jun. 2021, Art. no. e2021EA001670.

[3] B. Wu *et al.*, "Landing site selection and characterization of Tianwen-1 (Zhurong Rover) on Mars," *J. Geophys. Res., Planets*, vol. 127, no. 4, Apr. 2022, Art. no. e2021JE007137.

[4] W. X. Wan, C. Wang, C. L. Li, and Y. Wei, "China's first mission to Mars," *Nature Astron.*, vol. 4, no. 7, p. 721, Jul. 2020, doi: 10.1038/s41550-020-1148-6.

[5] J. B. Garvin, C. C. Schnetzler, J. J. Frawley, and S. E. H. Sakimoto, "Global geometric characteristics of fresh impact craters on Mars: A new perspective from the Mars Orbiter Laser Altimeter (MOLA)," *Meteoritics Planet. Sci.*, vol. 34, no. 4, p. A41, Jul. 1999.

[6] D. E. Smith *et al.*, "The global topography of Mars and implications for surface evolution," *Science*, vol. 284, no. 5419, pp. 1495–1503, May 1999, doi: 10.1126/science.284.5419.1495.

[7] A. S. McEwen *et al.*, "Mars reconnaissance Orbiter's high resolution imaging science experiment (HiRISE)," *J. Geophys. Res.*, vol. 112, no. E5, pp. 1–40, May 2007.

[8] Q. Y. Meng *et al.*, "High resolution imaging camera (HiRIC) on China's first Mars exploration Tianwen-1 mission," *Space Sci. Rev.*, vol. 217, no. 3, pp. 1–29, Apr. 2021.

[9] P.-E. Sarlin, D. DeTone, T. Malisiewicz, and A. Rabinovich, "SuperGlue: Learning feature matching with graph neural networks," in *Proc. IEEE/CVF Conf. Comput. Vis. Pattern Recognit. (CVPR)*, Jun. 2020, pp. 4937–4946, doi: 10.1109/CVPR42600.2020.00499.

[10] K. Gwinner *et al.*, "The high resolution stereo camera (HRSC) of Mars express and its approach to science analysis and mapping for Mars and its satellites," *Planet. Space Sci.*, vol. 126, pp. 93–138, Jul. 2016, doi: 10.1016/j.pss.2016.02.014.

[11] A. S. McEwen *et al.*, "The high resolution imaging science experiment (HiRISE) during MRO's primary science phase (PSP)," *Icarus*, vol. 205, no. 1, pp. 2–37, Jan. 2010, doi: 10.1016/j.icarus.2009.04.023.

[12] W. C. Liu and B. Wu, "An integrated photogrammetric and photoclinometric approach for illumination-invariant pixel-resolution 3D mapping of the lunar surface," *ISPRS J. Photogramm. Remote Sens.*, vol. 159, pp. 153–168, Jan. 2020.

[13] Z. Wang, *Principles of Photogrammetry (With Remote Sensing)*. Wuhan, China: Press of Wuhan Technical University of Surveying and Mapping, 1990.

[14] P. Yang *et al.*, "Orbit determination of China's first Mars probe Tianwen-1 during interplanetary cruise," *Adv. Space Res.*, vol. 69, no. 2, pp. 1060–1071, Jan. 2022, doi: 10.1016/j.asr.2021.10.046.

[15] D. G. Lowe, "Distinctive image features from scale-invariant keypoints," *Int. J. Comput. Vis.*, vol. 60, no. 2, pp. 91–110, Nov. 2004.

[16] K. Gwinner *et al.*, "Derivation and validation of high-resolution digital terrain models from Mars express HRSC data," *Photogrammetric Eng. Remote Sens.*, vol. 75, no. 9, pp. 1127–1142, Sep. 2009.

[17] H. Hu and B. Wu, "Block adjustment and coupled epipolar rectification of LROC NAC images for precision lunar topographic mapping," *Planet. Space Sci.*, vol. 160, pp. 26–38, Oct. 2018.

[18] J. Sun, Z. Shen, Y. Wang, H. Bao, and X. Zhou, "LoFTR: Detector-free local feature matching with transformers," 2021, *arXiv:2104.00680*.

[19] R. Li, J. Hwangbo, Y. Chen, and K. Di, "Rigorous photogrammetric processing of HiRISE stereo imagery for Mars topographic mapping," *IEEE Trans. Geosci. Remote Sens.*, vol. 49, no. 7, pp. 2558–2572, Jul. 2011.

[20] Z. Li, B. Wu, W. C. Liu, and Z. Chen, "Integrated photogrammetric and photoclinometric processing of multiple HRSC images for pixelwise 3-D mapping on Mars," *IEEE Trans. Geosci. Remote Sens.*, vol. 60, pp. 1–13, 2022, doi: 10.1109/tgrs.2021.3106737.

[21] X. Geng, Q. Xu, S. Xing, and C. Lan, "A generic pushbroom sensor model for planetary photogrammetry," *Earth Space Sci.*, vol. 7, no. 5, May 2020, Art. no. e2019EA001014, doi: 10.1029/2019EA001014.

[22] J. Grodecki and G. Dial, "Block adjustment of high-resolution satellite images described by rational polynomials," *Photogramm. Eng. Remote Sens.*, vol. 69, no. 1, pp. 59–68, Jan. 2003, doi: 10.14358/Pers.69.1.59.

[23] H. Hirschmüller, "Accurate and efficient stereo processing by semi-global matching and mutual information," in *Proc. IEEE Conf. Comput. Vis. Pattern Recognit.*, vol. 2, Jun. 2005, pp. 807–814.

[24] H. Hu, C. Chen, B. Wu, X. Yang, Q. Zhu, and Y. Ding, "Texture-aware dense image matching using ternary census transform," in *Proc. Congr., Commission*, 2016, vol. 3, no. 3, pp. 59–66.

[25] W. Chung Liu, B. Wu, and C. Wöhler, "Effects of illumination differences on photometric stereo shape-and-albedo-from-shading for precision lunar surface reconstruction," *ISPRS J. Photogramm. Remote Sens.*, vol. 136, pp. 58–72, Feb. 2018.

[26] A. Grumpe, F. Belkhir, and C. Wöhler, "Construction of lunar DEMs based on reflectance modelling," *Adv. Space Res.*, vol. 53, no. 12, pp. 1735–1767, Jun. 2014, doi: 10.1016/j.asr.2013.09.036.

[27] B. Wu, W. C. Liu, A. Grumpe, and C. Wöhler, "Construction of pixel-level resolution DEMs from monocular images by shape and albedo from shading constrained with low-resolution DEM," *ISPRS J. Photogramm. Remote Sens.*, vol. 140, pp. 3–19, Jun. 2018.

[28] H. Hu and B. Wu, "Planetary3D: A photogrammetric tool for 3D topographic mapping of planetary bodies," *ISPRS Ann. Photogramm., Remote Sens. Spatial Inf. Sci.*, vol. IV-2/W5, pp. 519–526, May 2019.

[29] D. DeTone, T. Malisiewicz, and A. Rabinovich, "SuperPoint: Self-supervised interest point detection and description," in *Proc. IEEE/CVF Conf. Comput. Vis. Pattern Recognit. Workshops (CVPRW)*, Jun. 2018, pp. 337–349.

[30] N. Carion, F. Massa, G. Synnaeve, N. Usunier, A. Kirillov, and S. Zagoruyko. (2020). *End-to-End Object Detection With Transformers*. [Online]. Available: https://doi.org/10.1007/978-3-030-58452-8_13

[31] L. He, X. Ren, Q. Gao, X. Zhao, B. Yao, and Y. Chao, "The connected-component labeling problem: A review of state-of-the-art algorithms," *Pattern Recognit.*, vol. 70, pp. 25–43, Oct. 2017.

[32] S. Agarwal, N. Snavely, S. M. Seitz, and R. Szeliski, "Bundle adjustment in the large," in *Computer Vision-ECCV*, vol. 6312. Berlin, Germany: Springer, 2010, pp. 29–42.

[33] M. Wang, F. Hu, and J. Li, "Epipolar resampling of linear pushbroom satellite imagery by a new epipolarity model," *ISPRS J. Photogramm. Remote Sens.*, vol. 66, no. 3, pp. 347–355, May 2011, doi: 10.1016/j.ISPRSjprs.2011.01.002.

[34] L. Ye and B. Wu, "Integrated image matching and segmentation for 3D surface reconstruction in urban areas," *Photogrammetric Eng. Remote Sens.*, vol. 84, no. 3, pp. 135–148, Mar. 2018, doi: 10.14358/Pers.84.3.135.

[35] D. E. Smith *et al.*, "Mars Orbiter Laser Altimeter: Experiment summary after the first year of global mapping of Mars," *J. Geophys. Res., Planets*, vol. 106, no. E10, pp. 23689–23722, 2001, doi: 10.1029/2000je001364.

[36] M. M. Mills, A. S. McEwen, and C. H. Okubo, "A preliminary regional geomorphologic map in utopia planitia of the Tianwen-1 zhurong landing region," *Geophys. Res. Lett.*, vol. 48, no. 18, Sep. 2021, doi: 10.1029/2021GL094629.

Zhaojin Li received the B.S. degree in remote sensing from Wuhan University, Wuhan, China, in 2019. She is currently pursuing the Ph.D. degree with a major in photogrammetry and remote sensing with The Hong Kong Polytechnic University, Hong Kong.

Her research interests include planetary mapping, photogrammetry, and computer vision.

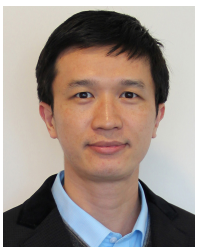

Bo Wu is currently a Professor with the Department of Land Surveying and Geo-Informatics, The Hong Kong Polytechnic University, Hong Kong. He is also a principal investigator (PI) of the project "Mars Landing Site—Topographic and Geomorphological Characterization and Analysis" funded by the China Academy of Space Technology, Beijing, China, and a Science Team Member of the Tianwen-1 Mars mission. His research interests are mainly in planetary remote sensing and photogrammetry.

Wai Chung Liu received the Ph.D. degree in photogrammetry and planetary mapping from The Hong Kong Polytechnic University, Hong Kong, in 2020.

He is currently a Post-Doctoral Fellow with The Hong Kong Polytechnic University. His research interests include planetary mapping and photometry, shape-from-shading, and photogrammetry.

Long Chen is currently pursuing the Ph.D. degree with a major in photogrammetry and remote sensing with The Hong Kong Polytechnic University, Hong Kong.

His research interests include real-time photogrammetry and image processing, 3-D mapping, and robotic vision.

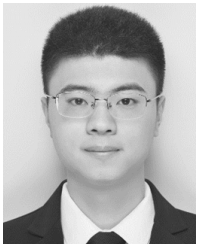

Hongliang Li is currently pursuing the Ph.D. degree with a major in planetary remote sensing and mapping with The Hong Kong Polytechnic University, Hong Kong.

His research interest focuses on planetary mapping, shape-from-shading, and photogrammetry.

Jie Dong is currently a Researcher with the China Academy of Space Technology, Beijing, China. He is also the Entry System Designer of the Tianwen-1 Mars probe.

Wei Rao is currently a Researcher with the China Academy of Space Technology, Beijing, China. He is also the Deputy Chief Designer of the Tianwen-1 Mars probe.

Dong Wang is currently a Researcher with the Changchun Institute of Optics, Fine Mechanics and Physics, Chinese Academy of Sciences, Beijing, China. He is also a System Designer of the HiRIC onboard the Tianwen-1 Mars probe.

Qingyu Meng is currently a Researcher with the Changchun Institute of Optics, Fine Mechanics and Physics, Chinese Academy of Sciences, Beijing, China. He is also a System Designer of the HiRIC onboard the Tianwen-1 Mars probe.

Jihong Dong is currently a Researcher with the Changchun Institute of Optics, Fine Mechanics and Physics, Chinese Academy of Sciences, Beijing, China. He is also the Chief Designer of the HiRIC onboard the Tianwen-1 Mars probe.